

# Effects of insoluble surfactants on breaking waves: regular and spilling regimes

B. Wang<sup>1</sup>, J. Chergui<sup>2</sup>, S. Shin<sup>3</sup>, D. Juric<sup>2,4</sup>, C. R. Constante-Amores<sup>1†</sup>

<sup>1</sup>Department of Mechanical Science and Engineering, University of Illinois, Urbana Champaign, IL 61801, USA

<sup>2</sup> Université Paris Saclay, Centre National de la Recherche Scientifique (CNRS), Laboratoire Interdisciplinaire des Sciences du Numérique (LISN), 91400 Orsay, France

<sup>3</sup>Department of Mechanical and System Design Engineering, Hongik University, Seoul 04066, Republic of Korea

<sup>4</sup>Department of Applied Mathematics and Theoretical Physics, University of Cambridge, Cambridge CB3 0WA, UK

We investigate the influence of insoluble surfactants on the spatio-temporal evolution of breaking waves, focusing on both regular and spilling regimes. Three-dimensional direct numerical simulations are conducted using an interface-tracking/level-set method that incorporates surfactant-induced Marangoni stresses. The simulations reveal that surfactant gradients, through Marangoni stresses, markedly alter the wave dynamics. While regular breakers exhibit only minor modifications in the presence of surfactants, increasing surfactant-induced Marangoni stresses in spilling breakers leads to pronounced changes in the crest evolution, vorticity generation, and even a transition towards plunging-like behavior. To quantify these effects, we also extend circulation-based theoretical frameworks to account for surfactant contributions. This work demonstrates the crucial role that surfactants play in the dynamics of breaking waves, revealing that their impact is primarily driven by Marangoni stresses rather than surface tension reduction.

## 1. Introduction

Surface wave breaking plays a significant role in the exchange of mass, momentum, and energy across the air-sea boundary (Melville 1996; Garbe *et al.* 2014; Iafrati 2009; Deike 2022). When waves break, they generate turbulence, entrain air, and enhance mixing, processes that significantly affect oceanic and atmospheric dynamics (Melville 1996; Deike 2022). The underlying physics of wave breaking, particularly spilling and plunging breakers, has been extensively studied using both experiments and numerical simulations (Rapp & Melville 1990; Chen *et al.* 1999; Duncan *et al.* 1999; Duncan 2001; Qiao & Duncan 2001; Liu & Duncan 2003, 2006; Iafrati 2009; Deike *et al.* 2015, 2016).

Early studies by Chen *et al.* (1999) showed that vorticity generation and energy dissipation are strongly localized near the wave crest, corroborating experimental observations of wave-induced turbulence. These findings, obtained through two-dimensional simulations, captured plunging and spilling breaker dynamics. Building on this, Iafrati (2009) provided a comprehensive numerical framework for analyzing the mechanics of both plunging and spilling breakers. Their work classified different wave regimes as a function of the initial wave steepness,  $\epsilon$ , for fixed Reynolds and Weber numbers ( $Re = 10^4$ ,  $We = 100$ ). Waves remained regular for  $\epsilon < 0.33$ ; transition to spilling breaker when  $0.33 \leq \epsilon < 0.37$  and

† Email address for correspondence: crconsta@illinois.edu

become plunging breakers for  $\epsilon \geq 0.37$ . These results agree with the theoretical analysis by Grue & Fructus (2010*a*). Building on earlier studies, Deike *et al.* (2015, 2016) used direct numerical simulations (DNS) to investigate the mechanisms of energy dissipation in breaking waves, highlighting differences between plunging and spilling regimes. Their work emphasized the transition to turbulence, vorticity generation, and air entrainment as central features of breaking dynamics.

Breaking waves undergo a cascade of processes, from jet impact and vortex formation to bubble entrainment and droplet ejection, that enhance mixing and momentum transfer across the interface (Liu & Duncan 2006; Deike 2022). High-fidelity simulations by Wang *et al.* (2016) captured the formation of bubbles, droplets, and spray, offering insight into the multiphase dynamics following wave impact. To model energy dissipation more broadly, Mostert & Deike (2020) developed a theoretical framework that relates dissipation rates to wave height, water depth, and beach slope. Their model was validated numerically and extended empirically to offshore conditions. In a follow-up work, Mostert *et al.* (2022) examined the transition from laminar to turbulent flow, showing that the energy dissipation rates and the size distributions of bubbles and droplets become independent of the Reynolds number once it exceeds a sufficiently high threshold. Recent studies have further examined the dynamics of plunging breakers, such as the work by Di Giorgio *et al.* (2022), who performed both two- and three-dimensional simulations across different Reynolds numbers, resolving the evolution of the air–water interface and associated bubble structures. Similarly, Hu *et al.* (2024) investigated the influence of wave slope and Reynolds number on spray formation and air entrainment during breaking.

Most of the recent studies on breaking waves have focused on clean, uncontaminated interfaces. However, natural surface-active agents (surfactants), which are ubiquitous in marine environments due to biological activity and pollution, are often present in the ocean surface (Lapham 1998; Laxague *et al.* 2024). Surfactants may be either insoluble (residing primarily at the air–water interface) or soluble (dissolved in the bulk fluid and can adsorb to and desorb from the interface). In both cases, spatial variations in concentration in the interface result in surface tension gradients, leading to Marangoni stresses driven flow from regions of low to high surface tension Manikantan & Squires (2020). Surfactant-driven Marangoni stresses can modify interfacial phenomena. For example, in capillary singularities, surfactant-induced flows can retard thread thinning and promote the formation of microthreads (Ambravaneswaran & Basaran 1999; Craster *et al.* 2002; Liao *et al.* 2006; Wee *et al.* 2020; Kamat *et al.* 2018; Constante-Amores *et al.* 2020). In small-scale systems related to wave breaking, such as bubbles and droplets, surfactants have been found to resist jet breakup, slow down the droplet ejection after the bursting of a bubble, and alter aerosol production (Takagi & Matsumoto 2011; Constante-Amores *et al.* 2021*c*; Ma *et al.* 2023).

Surfactants alter every stage of wave breaking, such as capillary wave formation, and the structure of the turbulent flow beneath the crest (Ceniceros 2003; Liu & Duncan 2006, 2007). Two-dimensional simulations of capillary waves with insoluble surfactant by Ceniceros (2003) showed that Marangoni stresses reduce both the bulge size and the wave amplitude while sharpening the toe curvature. Liu & Duncan (2003) and Liu & Duncan (2006) revealed similar trends with a suppression of capillary ripples, smoother crest evolution and a smaller, blunter bulge even at modest surfactant concentrations in wave-tank experiments on weak spilling breakers with the soluble surfactant (sodium dodecyl sulphate). By tracking the time varying bulge geometry, they linked these macroscopic changes directly to surface-rheological properties, concluding that surfactant-induced surface tension gradients delay toe shedding and reduce energy dissipation. Plunging breakers respond to the presence of surfactants even more dramatically. Erinin *et al.*

(2023) did experiments with Triton X-100 and surfactant-depleted water, and showed that surfactants deform the jet tip, fragment the entrained air cavity, and weaken the downward plunge. They also presented numerical simulations that modeled surfactants as tracer particles along the interface. While these confirmed the qualitative trends, they could not capture the fully coupled surfactant-induced Marangoni stresses. Extending this work, Liu *et al.* (2025) demonstrated that soluble surfactants reduce both droplet count and ejection velocity while shifting the size distribution towards larger diameters. Together, these studies establish that even trace amounts of surfactants suppress small scale capillary activity, delay the onset of turbulence beneath the crest and reshape the air entrainment and spray signature of breaking waves.

As revealed by the foregoing review, considerable progress has been made in understanding the role of surfactants in breaking wave dynamics. However, to the best of our knowledge, the specific influence of surfactant-induced Marangoni stresses remains poorly understood. In this study, we investigate the influence of insoluble surfactants on breaking wave dynamics, with a particular focus on regular and spilling regimes, using direct numerical simulations. The rest of this paper is structured as follows: in Section 2, the numerical method, governing dimensionless parameters, problem configuration, and validation, are introduced. Section 3 presents the results, and concluding remarks are given in Section 4.

## 2. Problem formulation and numerical method

High resolution simulations were performed by solving the two-phase incompressible Navier-Stokes equations with surface tension in a three-dimensional Cartesian domain  $\mathbf{x} = (x, y, z)$  (see Figure 1). The interface between the gas and liquid is described by a hybrid front-tracking/level-set method, where (insoluble) surfactant transport is explicitly resolved at the interface (Shin *et al.* 2018). Here, and in what follows, all variables are made dimensionless (represented by tildes) using the following characteristic scales

$$\tilde{\mathbf{x}} = \frac{\mathbf{x}}{\lambda}, \quad \tilde{t} = \frac{t}{t_r}, \quad \tilde{\mathbf{u}} = \frac{\mathbf{u}}{c}, \quad \tilde{p} = \frac{p}{\rho_l c^2}, \quad \tilde{\sigma} = \frac{\sigma}{\sigma_s}, \quad \tilde{\Gamma} = \frac{\Gamma}{\Gamma_\infty}, \quad (2.1)$$

where,  $t$ ,  $\mathbf{u}$ , and  $p$  stand for time, velocity, and pressure, respectively. The physical parameters correspond to the liquid density,  $\rho_l$ , liquid viscosity,  $\mu_l$ , and surfactant-free surface tension,  $\sigma_s$ . The characteristic velocity is  $c = \sqrt{g\lambda}$  with  $\lambda$  the wavelength of the wave; hence, the characteristic time scale is  $t_r = \lambda/c$ . The interfacial surfactant concentration,  $\Gamma$ , is scaled by the saturation interfacial concentration,  $\Gamma_\infty$ . As a result of this scaling, the dimensionless equations read

$$\nabla \cdot \tilde{\mathbf{u}} = 0, \quad (2.2)$$

$$\begin{aligned} \tilde{\rho} \left( \frac{\partial \tilde{\mathbf{u}}}{\partial \tilde{t}} + \tilde{\mathbf{u}} \cdot \nabla \tilde{\mathbf{u}} \right) + \nabla \tilde{p} = & - \frac{\mathbf{i}_z}{Fr^2} + \frac{1}{Re} \nabla \cdot [\tilde{\mu} (\nabla \tilde{\mathbf{u}} + \nabla \tilde{\mathbf{u}}^T)] + \\ & + \frac{1}{We} \int_{\tilde{A}(\tilde{t})} (\tilde{\sigma} \tilde{\kappa} \mathbf{n} + \nabla_s \tilde{\sigma}) \delta(\tilde{\mathbf{x}} - \tilde{\mathbf{x}}_f) d\tilde{A}, \end{aligned} \quad (2.3)$$

$$\frac{\partial \tilde{\Gamma}}{\partial \tilde{t}} + \nabla_s \cdot (\tilde{\Gamma} \tilde{\mathbf{u}}_t) = \frac{1}{Pe_s} \nabla_s^2 \tilde{\Gamma}, \quad (2.4)$$

where the density and viscosity are given by  $\tilde{\rho} = \rho_g/\rho_l + (1 - \rho_g/\rho_l) \mathcal{H}(\tilde{\mathbf{x}}, \tilde{t})$  and  $\tilde{\mu} = \mu_g/\mu_l + (1 - \mu_g/\mu_l) \mathcal{H}(\tilde{\mathbf{x}}, \tilde{t})$  wherein  $\mathcal{H}(\tilde{\mathbf{x}}, \tilde{t})$  represents a Heaviside function, which is

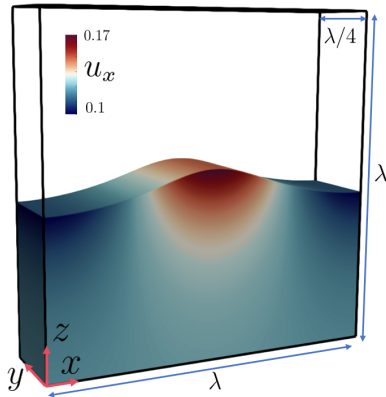


Figure 1: Schematic representation of the flow configuration. Initial configuration showing the computational domain in a 3D Cartesian coordinate system,  $\mathbf{x} = (x, y, z)$ .

zero in the gas phase and unity in the liquid phase, while the subscript ‘ $g$ ’ and ‘ $l$ ’ designate the gas, and liquid phases, respectively, and  $\tilde{\mathbf{u}}_t = (\tilde{\mathbf{u}}_s \cdot \mathbf{t}) \mathbf{t}$  is the tangential velocity at the interface in which  $\tilde{\mathbf{u}}_s$  represents the interfacial velocity, and  $\kappa$  is the curvature, and  $\mathbf{t}$  is the unit tangent vector to the interface. The interfacial gradient is given by  $\nabla_s = (\mathbf{I} - \mathbf{nn}) \cdot \nabla$  wherein  $\mathbf{I}$  is the identity tensor and  $\mathbf{n}$  is the outward-pointing unit normal. In addition,  $\delta$  is a Dirac delta function, equal to unity at the interface and zero otherwise, and  $\tilde{A}(\tilde{t})$  is the time-dependent interface area. As justified by the final paragraph of Stone (1990), in our frame of reference  $\mathbf{u} \cdot \mathbf{n} = 0$ , which gives rise to equation 2.4.

The dimensionless groups that appear in the governing equations are defined as

$$Re = \frac{\rho_l U \lambda}{\mu_l}, \quad We = g^{1/2} \lambda \sqrt{\frac{\rho_l}{\sigma_s}}, \quad Fr = \frac{c}{\sqrt{g \lambda}}, \quad Pe_s = \frac{c \lambda}{\mathcal{D}_s}, \quad \beta_s = \frac{\Re \mathcal{T} \Gamma_\infty}{\sigma_s}, \quad (2.5)$$

where  $Re$ ,  $We$ ,  $Fr$ , and  $Pe_s$  stand for the Reynolds, Weber, Froude, and (interfacial) Peclet numbers. The parameter  $\beta_s$  is the surfactant elasticity number that is a measure of the sensitivity of the surface tension,  $\sigma$ , to the interface surfactant concentration,  $\Gamma$ . Here,  $\Re$  is the ideal gas constant value ( $\Re = 8.314 \text{ J K}^{-1} \text{ mol}^{-1}$ ),  $\mathcal{T}$  denotes temperature, and  $\mathcal{D}_s$  stands for the interfacial diffusion coefficient.

The non-linear Langmuir equation is used to describe  $\sigma$  in terms of  $\Gamma$ , this is

$$\tilde{\sigma} = \max[0.05, 1 + \beta_s \ln(1 - \tilde{\Gamma})], \quad (2.6)$$

where a lower limit of  $\sigma$  has been set to 0.05, below which the Langmuir equation of state may diverge. Finally, the Marangoni stress,  $\tilde{\tau}$ , is expressed as a function of  $\tilde{\Gamma}$  as

$$\frac{1}{We} \nabla_s \tilde{\sigma} \cdot \mathbf{t} \equiv \frac{\tilde{\tau}}{We} = - \frac{Ma}{(1 - \tilde{\Gamma})} \nabla_s \tilde{\Gamma} \cdot \mathbf{t}, \quad (2.7)$$

where  $Ma = \beta_s / We = Re \mathcal{T} \Gamma_\infty / \rho_l U^2 \lambda$  is the Marangoni parameter. Tildes are dropped henceforth.

### 2.1. Numerical Setup and parameters

In this work, we study the evolution of a single breaking wave with wavelength  $\lambda$ . The computational domain is defined as  $(\lambda \times \lambda/4 \times \lambda)$ , as shown in figure 1. While previous studies have commonly employed cubic domains of size  $\lambda^3$ , the reduced spanwise

extent adopted here is intentional, as we are not focusing on the strongly 3D dynamics associated with the plunging regime. By reducing the spanwise dimension, we limit the computational cost while retaining 3D dynamics. This approach has also been adopted by Di Giorgio *et al.* (2024). The wave propagates in the  $x$ -direction with periodic boundary conditions in both the streamwise ( $x$ ) and spanwise ( $y$ ) directions. No-slip and no-penetration conditions are applied at the bottom boundary. We emphasize that the chosen spanwise extent is sufficient to capture the essential dynamics of the breaking wave while maintaining computational efficiency.

The initial free-surface profile  $\eta(x, y)$  follows the previous work from Chen *et al.* (1999) and Iafrati (2009), which corresponds to a third-order Stokes wave solution that neglects depth effects and secular terms, computed up to third order in the wave amplitude  $a$ . The surface elevation is prescribed as

$$\eta(x, y) = \frac{a}{\lambda} \left( \cos(kx) + \frac{1}{2}\varepsilon \cos(2kx) + \frac{3}{8}\varepsilon^2 \cos(3kx) \right), \quad (2.8)$$

where  $k = 2\pi/\lambda$  is the wavenumber, and  $\varepsilon = ak$  is the initial wave steepness. As noted by Iafrati (2009), the omission of the secular term has a negligible effect on the resulting dynamics; we therefore adopt this initialization and focus on surfactant-induced effects. The initial velocity field is obtained under the assumption of a free surface (e.g., negligible air pressure). The velocity profile in the water is derived from the velocity potential associated with the free-surface profile and is expressed as

$$u = \Omega a e^{kz} \cos(kx), \quad v = \Omega a e^{kz} \sin(kx), \quad (2.9)$$

where  $\Omega = \sqrt{gk(1 + \varepsilon^2)}$  accounts for the nonlinear correction by removing higher order terms (Whitham 2011; Iafrati 2009). We note that other studies have considered more physically detailed conditions, in which a velocity profile in the air is also defined (Mostert *et al.* 2022). Finally, we note that surface tension forces are not included in the initializations, but their influence will become relevant once the wave propagates in the streamwise direction.

The dimensionless parameters used in this study are consistent with experimentally realizable systems. The density and viscosity ratios are set to  $\rho_g/\rho_l = 1/850$  and  $\mu_g/\mu_l = 17.4 \times 10^{-6}/8.9 \times 10^{-4} = 1.96 \times 10^{-2}$ , respectively, based on standard properties of air and water. The water depth is set to  $h = \lambda/2$ , consistent with the configuration used by Deike *et al.* (2018), who showed that this ratio has minimal influence on wave evolution in the regimes of interest. Following Iafrati (2009), we fix the Weber and Reynolds numbers at  $We = 100$  and  $Re = 10^4$ . The chosen Weber number corresponds to water waves with a wavelength of approximately 27 cm, corresponding to Reynolds number of  $Re \approx 4.4 \times 10^5$ . Resolving flows at such high Reynolds would require prohibitively fine resolution, which is not feasible within the constraints of our fixed-grid approach. While adaptive mesh refinement has enabled higher Re simulations in other studies (Deike *et al.* 2018; Mostert *et al.* 2022), our focus is limited to regular and weakly spilling breakers. The chosen parameters therefore strike a balance between computational feasibility and physical realism, while capturing the dominant surfactant-laden dynamics. In this work, we have considered insoluble surfactants whose critical micelle concentration (CMC), i.e.  $\Gamma_\infty \sim \mathcal{O}(10^{-6})$  mol m $^{-2}$  for NBD-PC (1-palmitoyl-2-12-[(7-nitro-2-1,3-benzoxadiazol-4-yl)amino]dodecanoyl-sn-glycero-3-phosphocholine); thus, we have explored the range of  $0.1 < \beta_s < 0.9$  which corresponds to  $\mathcal{O}(10^{-7}) < \text{CMC} < \mathcal{O}(10^{-6})$  mol m $^{-2}$ , for typical values of  $\sigma_s$ . We have set  $Pe_s = 10^3$  following Batchvarov *et al.* (2020) and Constante-Amores *et al.* (2020), who showed that the interfacial dynamics are weakly-dependent on  $Pe_s$  beyond this value. Finally, the initial concentration of the surfactant-laden cases

---

$\epsilon$	$\beta_s$	Regular	Spilling	Plunging
0.3	Surfactant-free	X		
0.3	0.5	X		
0.3	0.9	X		
0.324	Surfactant-free		X	
0.324	0.5		X	
0.324	0.9		X	
0.33	Surfactant-free		X	
0.33	0.5			X
0.33	0.9			X
0.35	Surfactant-free		X	
0.35	0.5			X
0.35	0.9			X
0.37	Surfactant-free			X

---

Table 1: Wave behavior as a function of wave steepness  $\epsilon$  and surfactant parameter  $\beta_s$ .

---

$c$  considered here are set to  $\Gamma = \Gamma_\infty/2$ , as previous work by Constante-Amores *et al.* (2020, 2023b)

The simulations presented here are mesh independent. A resolution of  $\lambda/\Delta\mathbf{x} = 512$  was found sufficient to ensure that further mesh refinement does not alter the numerical results. This resolution is consistent with that used in previous studies at the same dimensionless parameters (Iafrati 2009). We also note that the simulations in the plunging regime are terminated upon the onset of plunging. Although the numerical framework is capable of resolving post-breaking behavior, this is not the focus of the current study. Further investigation would require refining the simulations, which would significantly increase computational cost, and subsequently, we do not explore this avenue here.

The numerical validation of the surfactant equations has been previously presented in Shin *et al.* (2018). Extensive mesh studies for surface-tension-driven phenomena using the same computational method can be found elsewhere, e.g. (Batchvarov *et al.* 2021, 2020; Constante-Amores *et al.* 2020, 2021b, 2022, 2023a). Additionally, liquid volume and surfactant mass conservation are met under errors of less than  $10^{-1}\%$ , and  $10^{-2}\%$ , respectively.

### 3. Results

Table 1 summarizes the observed wave behavior as a function of the steepness parameter  $\epsilon$  with  $Re = 10^4$  and  $We = 100$ . We observe that for surfactant-free cases, the wave remains regular for  $\epsilon = 0.3$ , transitions to a spilling-type breakup for  $\epsilon = 0.324$ , and finally exhibits plunging-type breakup for  $\epsilon = 0.37$ . These findings agree with previous work by Iafrati (2009) and Grue & Fructus (2010b). We have included simulations with  $\epsilon = 0.324$ , which aligns with the onset from regular to spilling-type breaking predicted when accounting for the secular growth term  $\epsilon^3/8$  by Grue & Fructus (2010b). It should be noted that for  $\epsilon = 0.37$ , the simulation was terminated just prior to the breakup. This choice was made to focus the analysis on the wave behavior leading up to the event. A detailed study of the post-breakup dynamics in the plunging regime is beyond the scope of this study.

To investigate the role of wave breaking in energy dissipation, we track the temporal evolution of the kinetic energy. Figure 2 presents the kinetic energy, defined as  $E_k =$

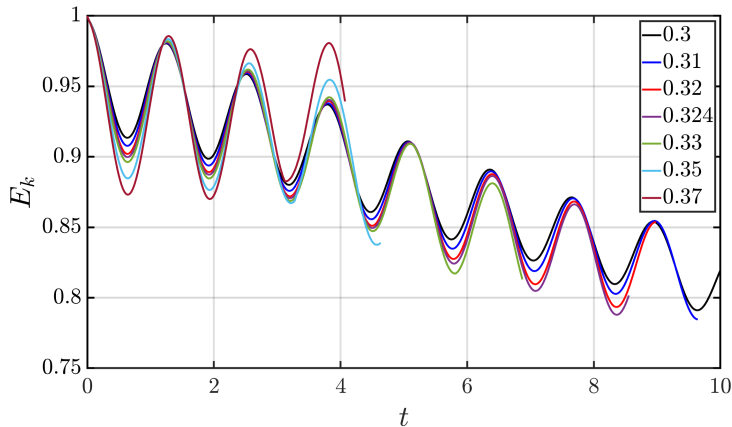


Figure 2: Temporal evolution of the kinetic energy as a function of the wave steepness  $\epsilon$  in surfactant-free conditions.

$\rho \int_v \mathbf{u}^2/2dV$ , normalized by its initial value, as a function of the initial wave steepness  $\epsilon$ . The figure reveals distinct trends corresponding to the different breaking regimes, highlighting the increasing intensity of energy decay with more intense wave breaking. In the regular wave regime, a nearly constant decay rate is observed. The theoretical decay of mechanical energy due to viscous damping is given by  $E_{mech}(t) = E_{mech}(0)e^{-2\gamma t}$ , where  $E_{mech}$  is the mechanical energy (e.g., equal to twice the kinetic energy for small-amplitude waves) and  $\gamma = 2k^2\mu_l/\rho_l$  is the damping coefficient (Landau & Lifshitz 1987). For the wave with steepness  $\epsilon = 0.3$ , the numerical simulation results in  $\gamma = 0.0091$ , which is in good agreement with the theoretical estimate  $\gamma \approx 0.0079$ . At higher steepness  $\epsilon = 0.37$ , a monotonic decrease in kinetic energy is observed, preceded by a phase of increasing amplitude and enhanced dissipation. Although the simulation is terminated just before the onset of plunging-type breakup, the flow already exhibits intensified velocities and steep velocity gradients near the interface, resulting in large kinetic energy and enhanced energy dissipation.

The changes in wave morphology that accompany these energy dissipation trends are illustrated in figure 3a-c, which show the spatiotemporal evolution of the interface in the  $(x-z)$  plane at  $y = \lambda/8$  for initial steepness values  $\epsilon = [0.3, 0.324, 0.33]$ . At  $\epsilon = 0.3$ , the wave evolution remains regular over time. As the steepness increases to  $\epsilon = 0.324$ , weak signs of spilling emerge in the surfactant-free case, which become more pronounced at  $\epsilon = 0.33$ , where the formation of a forward-facing bulge near the wave crest marks the onset of spilling. The leading edge of this bulge, known as the toe, curves inward due to surface tension effects, consistent with the mechanism described by Duncan (2001). Capillary waves are also formed upstream of the toe, as reported by Duncan *et al.* (1999).

Figure 3(d-i) shows the effect of insoluble surfactants on the wave dynamics. At  $\epsilon = 0.3$  (see panels 3d-g), the addition of surfactant produces minimal changes compared to the surfactant-free case. This is expected, as the steepness remains below the critical value for Stokes waves ( $\epsilon_c \approx 0.32$ ); although surfactants reduce the surface tension, it is insufficient to generate a noticeable wave deformation. Once the wave enters the spilling regime ( $\epsilon = 0.324$ ), the presence of surfactant enhances the spilling behavior, with the effect being more pronounced at higher values of  $\beta_s$  (see panels 3e and 3h). For  $\epsilon = 0.33$ , a clear transition from spilling to plunging is observed in the case with  $\beta_s = 0.9$  (see panel

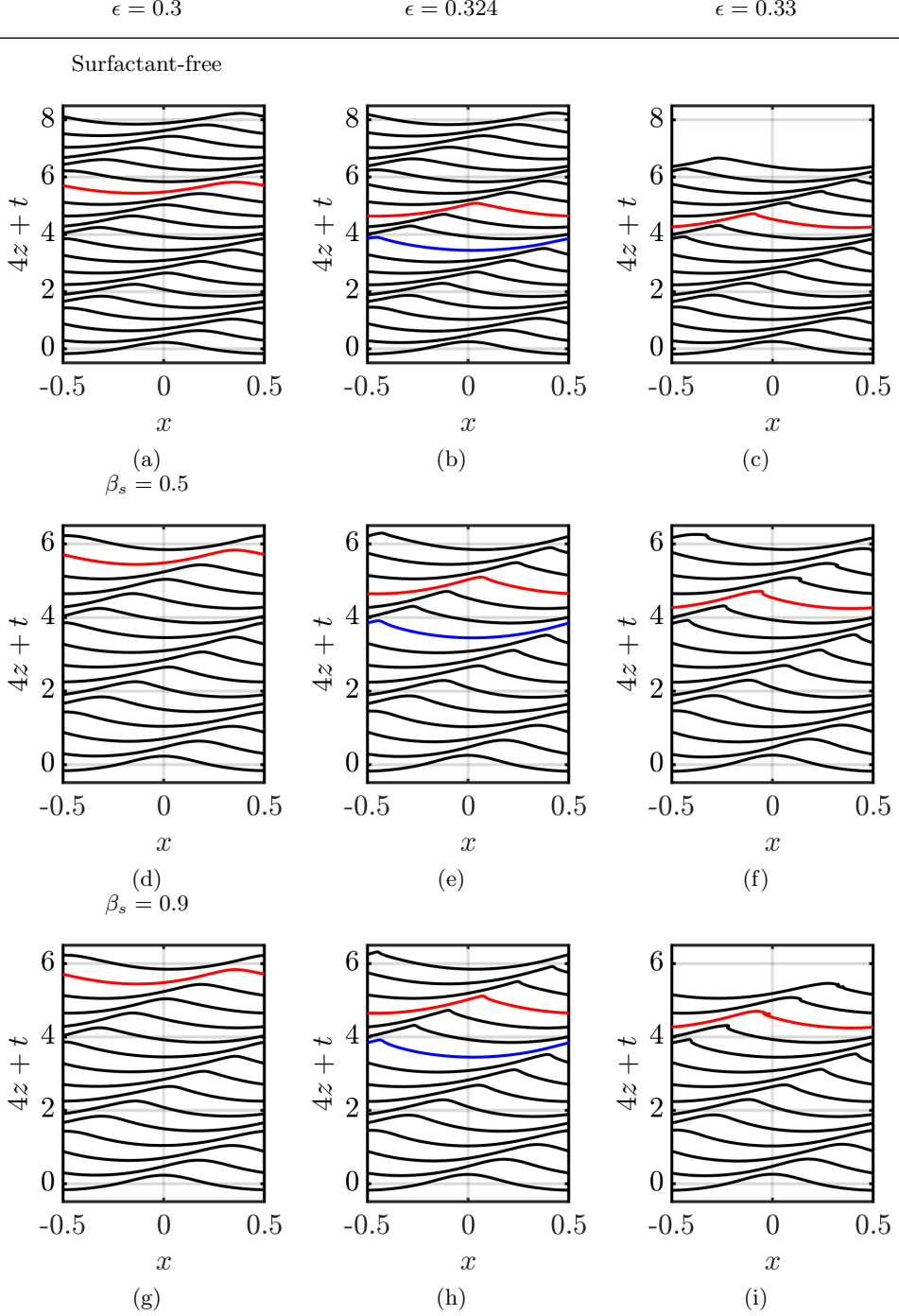


Figure 3: Time-space plots of the interface in the  $(x - z)$  plane ( $y = \lambda/8$ ) at equal time intervals for varying wave steepness  $\epsilon$ , and surfactant elasticity  $\beta_s$ . The vertical coordinates ( $y$ -axis) are stretched by a factor of 4 and shifted upward by the corresponding time to better illustrate the interface evolution. Colored lines mark selected times analyzed in detail below.



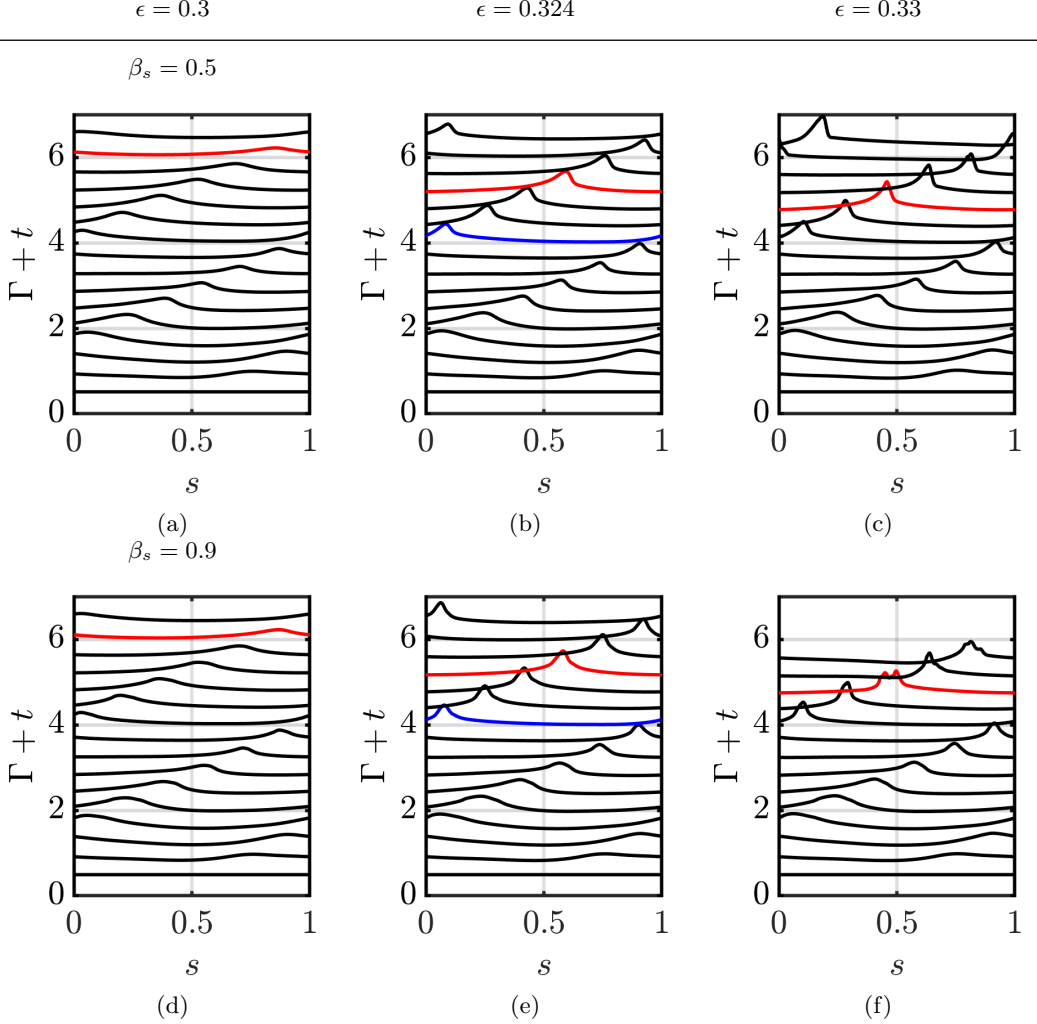


Figure 4: Time-space plots of normalized surfactant concentration  $\Gamma$  at time intervals as a function of the steepness  $\epsilon$ , and  $\beta_s$ . The data are plotted against arclength  $s \in [0, 1]$ , with vertical coordinates representing the normalized surfactant concentration  $\Gamma$  shifted by the corresponding time to clearly show the evolution of surfactant distribution. All cases end at  $t = 6$ , except the case for  $\epsilon = 0.33$  and  $\beta_s = 0.9$ , which breaks early ends at  $t = 5.2$ . For the surfactant-laden cases,  $Pe_s = 10^3$  and  $\Gamma = \Gamma_\infty/2$ . Colored lines mark selected times analyzed in detail below.

3i). This transition is driven by surfactant-induced Marangoni stresses, which arise from the non-uniform distribution of surfactant along the interface. These stresses modify the interfacial tension and promote localized accelerations, ultimately intensifying the wave-breaking process.

To elucidate the coupling between the interface dynamics and surfactant concentration, figure 4 presents the spatiotemporal evolution of  $\Gamma$  at the same time as in figure 3. A clear correlation emerges between the interfacial shape and the distribution of  $\Gamma$ . As the wave evolves, surfactant initially accumulates at troughs due to surface convergence,

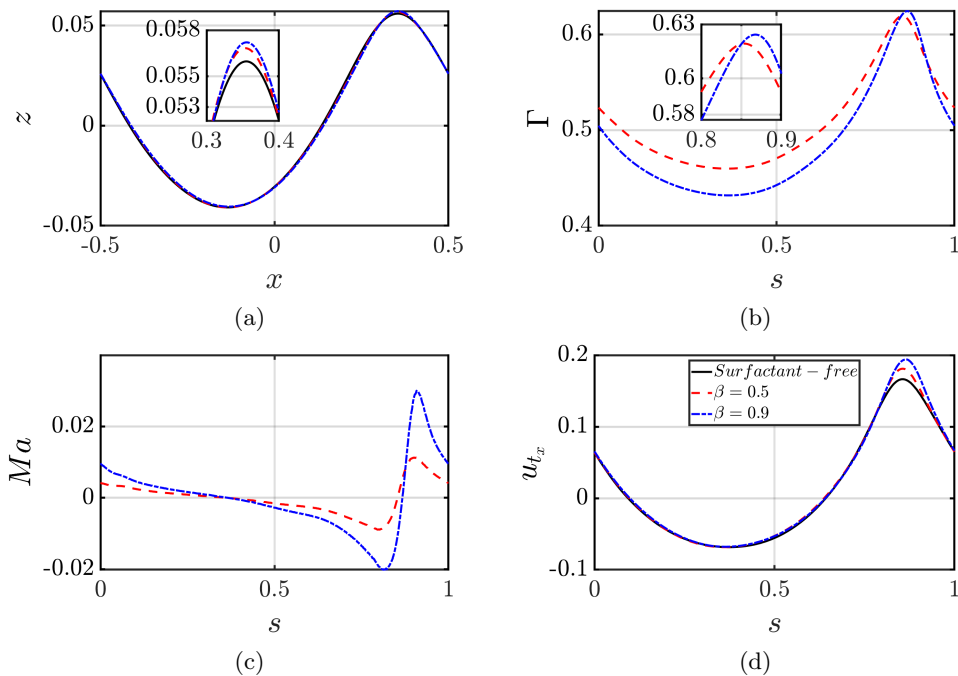


Figure 5: Effect of the elasticity parameter  $\beta_s$  for regular wave regime ( $\epsilon = 0.3$ ) at  $t = 5.6$ . Two-dimensional projections of the interface,  $\Gamma$ ,  $Ma$  and  $u_{tx}$  in the  $(x-z)$  plane ( $y = \lambda/8$ ) are shown in (a–d), respectively. Note that the abscissa in (a) corresponds to the  $x$  coordinate, and in (b–d) to the arc length,  $s$ .

then shifts toward the crests (where the interface exhibits divergent flow). Once the crest is formed, the local flow divergence redistributes  $\Gamma$ , causing it to diffuse away gradually. Comparing cases with  $\beta_s = 0.5$  and  $\beta_s = 0.9$ , the crest in the higher  $\beta_s$  leans forward more prominently, indicative of surfactant-induced modifications to the interfacial dynamics and wave deformation. The most pronounced surfactant concentration peak occurs in the  $\epsilon = 0.33$  case, indicative of strong Marangoni effects arising from steep surfactant gradients. Notably, in the case with  $\beta_s = 0.9$  and  $\epsilon = 0.33$ , two distinct peaks in  $\Gamma$  appear at later times, suggesting that the presence of surfactant has modified the interfacial shape, thereby altering the surface velocity field and leading to a subsequent redistribution of surfactant along the interface. This phenomenon is analyzed further below.

We now examine the coupling between the interface location, surfactant concentration  $\Gamma$ , Marangoni stress, and tangential velocity in the streamwise direction  $u_{tx}$ . To elucidate the underlying mechanisms, we select representative time instances at which wave features are most pronounced. These times, corresponding to different steepness regimes, are indicated in different colors in figure 3 and 4. We begin with the regular wave regime. For  $\epsilon = 0.3$ , figure 5a shows that the presence of surfactant has a minimal effect on the interface location at late times ( $t = 5.6$ ). However, figure 5b reveals that the surfactant concentration peaks at the wave crest, where surface tension is locally minimized. The resulting Marangoni stresses, driven by surface tension gradients, generate outward tangential flow away from the crest—i.e.,  $Ma > 0$  on the forward part of the crest and  $Ma < 0$  on the rear part of it. These Marangoni stresses act to suppress further

steepening of the wave by opposing interfacial deformation, thereby reducing the wave amplitude at late times (not shown). The influence of Marangoni stresses on the surface flow is evident in figure 5d, which shows that  $u_{tx}$  is significantly enhanced near the crest in the presence of surfactants, compared to the clean case, particularly for the high elasticity case ( $\beta_s = 0.9$ ). Despite the enhanced tangential velocity and the non-uniform surfactant distribution, the interface displacement remains small at this particular time. At  $\epsilon = 0.3$ , the inertial forces associated with wave propagation are insufficient to drive significant interface deformation or wave overturn, and the flow remains in a weakly nonlinear regime, where the balance between gravity and surface tension dominates. Moreover, surface tension remains relatively strong and effectively resists interface steepening. As a result, the Marangoni-induced tangential flow primarily redistributes momentum along the interface without producing noticeable changes in the wave shape.

We next consider the spilling regime; the interfacial location,  $\Gamma$ ,  $Ma$  and  $u_{tx}$  are shown in figure 6. For  $\epsilon = 0.324$ , the addition of surfactant significantly modifies the shape and position of the wave crest (see figure 6a). Surfactants also accumulate near the wave crest, leading to a noticeably sharper, and more forward-leaning profile (figure 6b). This effect becomes more pronounced with increasing surfactant elasticity, which enhances interfacial gradients and promotes stronger Marangoni stresses. The resulting non-uniform surfactant distribution leads to localized peaks in Marangoni stresses near the crest (figure 6c), and larger tangential velocities  $u_t$  (figure 6d). At higher elasticity ( $\beta_s = 0.9$ ),  $Ma$  enhance the spilling regime. These observations are in agreement with the experimental observations of Liu & Duncan (2006). At slightly higher steepness,  $\epsilon = 0.33$ , the addition of surfactant induces significant changes in the interfacial dynamics at  $t = 4.4$ . As shown in figure 6e, a small forward jet forms near the crest, initiating overturning of the interface. These features indicate a surfactant-driven transition from the spilling to plunging regime, particularly evident for the high elasticity  $\beta_s = 0.9$ . We observe the same behavior for  $\beta_s = 0.5$  at long times (not shown). The formation of this forward jet significantly reshapes both the surfactant concentration and tangential velocity fields. For  $\beta_s = 0.9$ , the surfactant distribution profile (figure 6f) develops two distinct surfactant peaks: a primary peak at the wave crest, where surfactant accumulates due to converging interfacial flow, and a secondary peak near the tip of the forward jet. Between these two peaks, a local minimum in  $\Gamma$  forms in the region of maximum jet curvature, where the interface begins to overturn. This minimum reflects a local surfactant depletion zone driven by the competition between inertial ejection and Marangoni-driven redistribution of surfactant. The resulting surfactant gradient enhances the Marangoni stress (figure 6g), promoting jet elongation. Figure 6h shows the tangential velocity field  $u_{tx}$  along the interface. The surfactant-free case exhibits a smooth, forward-directed surface flow. For  $\beta_s = 0.5$ , a small positive peak in  $u_{tx}$  appears just past the crest, indicating a moderate surfactant-induced modification to the surface flow. In contrast, the  $\beta_s = 0.9$  case displays a localized reversal in  $u_{tx}$  near the crest. This reversal is attributed to a combination of wave overturning—which alters the surface orientation and flow direction—and strong Marangoni stresses associated with steep surfactant concentration gradients.

Finally, in figure 7, we examine the effect of surfactant in greater detail by analyzing the tangential velocity in the reference frame of the wave crest for both surfactant-free and surfactant-laden cases with  $\epsilon = 0.9$  and  $\beta_s = 0.9$  at  $t = [3.6, 3.8, 4.0]$ . These times are selected to capture the onset of the transition from a spilling-like to a plunging regime. In the clean case, the tangential velocity relative to the crest,  $u_{tx} - c$ , is positive, indicating that the interfacial fluid is moving forward relative to the crest (see figure 7a-c). In contrast, in the surfactant-laden case,  $u_{tx} - c$  becomes negative, showing that

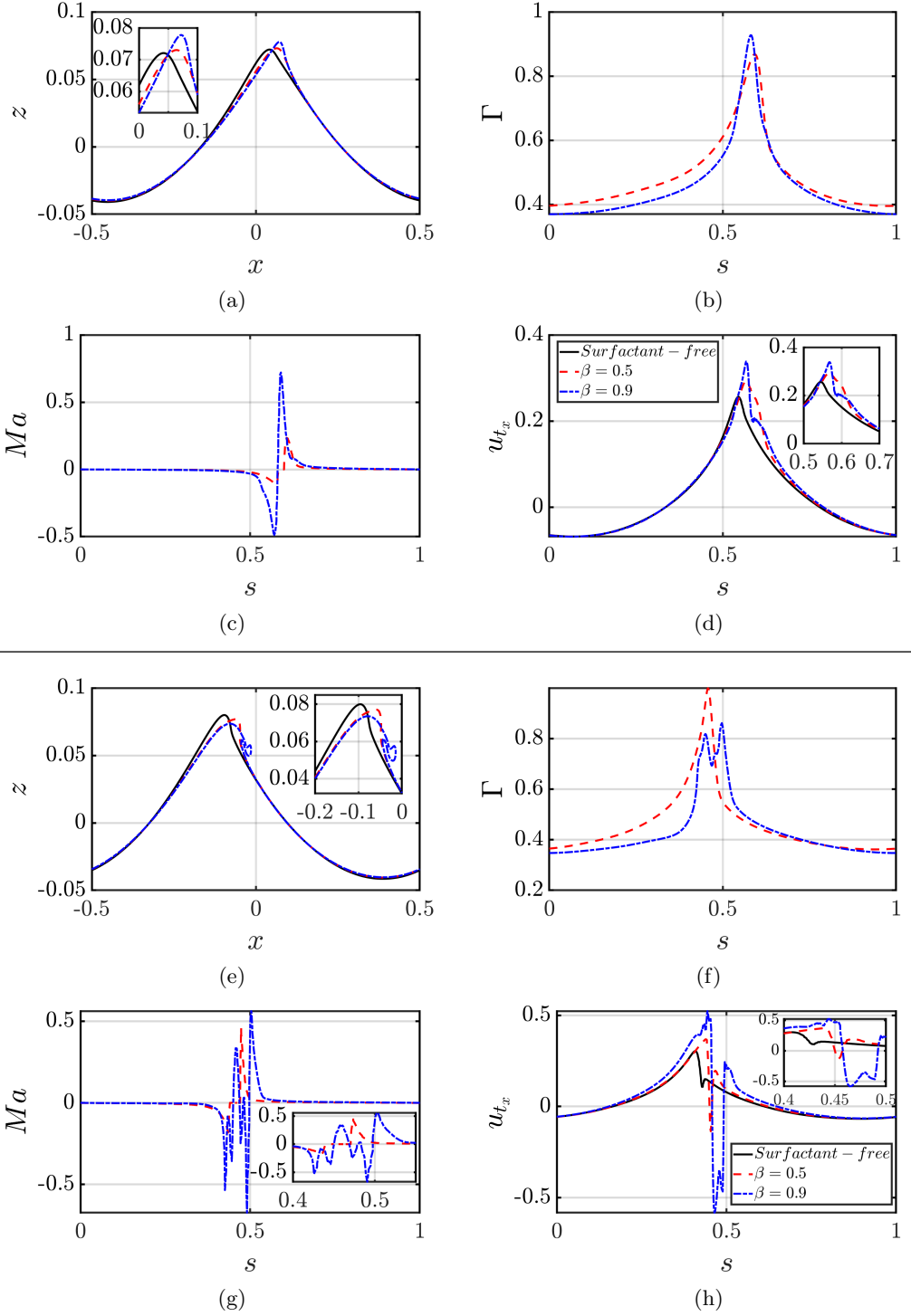


Figure 6: Effect of the elasticity parameter for the spilling regime for  $\epsilon = 0.324$  at  $t = 4.8$ , and  $\epsilon = 0.33$  at  $t = 4.4$ . Two-dimensional projections of the interface,  $\Gamma$ ,  $Ma$  and  $u_{t_x}$  in the  $(x-z)$  plane ( $y = \lambda/8$ ) are shown. Panels (a-d) correspond to  $\epsilon = 0.324$ , and panels (e-h) to  $\epsilon = 0.33$ .

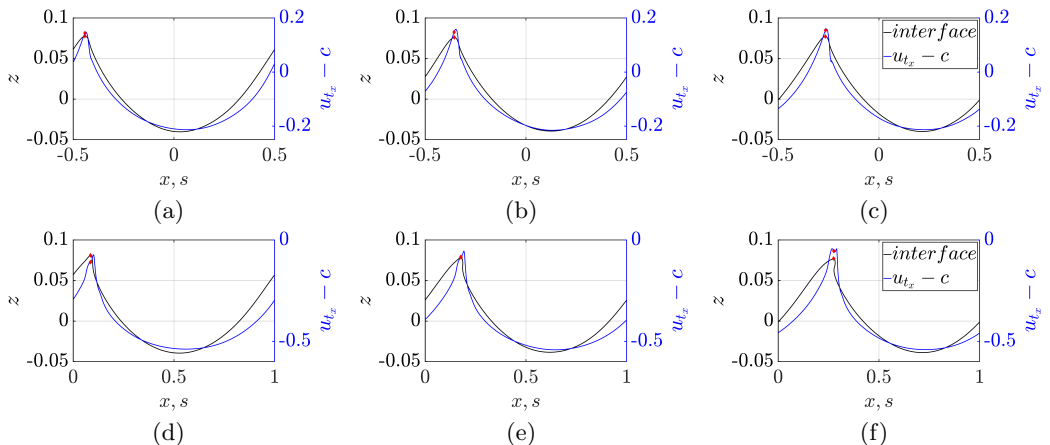


Figure 7: Two-dimensional projections of the interface location and tangential velocity in the reference frame of the wave crest for surfactant-free (top panels) with  $\epsilon = 0.33$ , and surfactant-laden case with  $\beta_s = 0.9$  (bottom panels) at times  $t = [3.6, 3.8, 4.0]$ , corresponding to columns one-to-three, respectively.

the interfacial fluid moves more slowly than the crest and effectively lags behind it. This change in the sign of the tangential velocity is a direct consequence of surfactant-driven Marangoni stresses arising from surfactant accumulation at the crest. These stresses drive a backward flow toward the trough, which sharpens the crest, promotes overturning, and triggers the transition from a spilling to a plunging regime.

To isolate the role of Marangoni stresses in the transition from the spilling-like to plunging regime, we perform additional simulations in which Marangoni stresses are suppressed by imposing  $\nabla_s \sigma = 0$  in equation 2.3. This constraint allows surfactant to remain non-uniformly distributed along the interface while preventing the generation of Marangoni stresses. Figure 8 presents results for the spilling cases discussed above. A comparison of the interface positions in the  $(z-x)$  plane reveals that Marangoni stresses induce a forward lean of the crest relative to the Marangoni stress-free cases, for both  $\epsilon = 0.324$  and  $\epsilon = 0.33$  (see figures 8a and 8d). When Marangoni stresses are active, a more uniform surfactant distribution is sustained (see figures 8b,e) by enhanced tangential velocities driven flow from high to low surfactant concentration regions, reflecting more efficient surfactant redistribution along the interface (see figures 8c,f). When Marangoni stresses are suppressed, tangential velocities drop significantly; this reduction arises not only from the absence of Marangoni-driven flow but also from the accompanying decrease in mean surface tension, which weakens the capillary forces and reduces interfacial shear. The weaker capillary forces result in diminished interfacial shear, suppressing jet formation and spilling breakup. Therefore, the onset of the spilling-to-plunging transition is driven by Marangoni stresses rather than reduced surface tension.

Figure 9 shows the spanwise vorticity  $\omega_y = (\nabla \times \mathbf{u})_y$  in a  $(x-z)$  plane overlaid with the interface shape for steepness,  $\epsilon = 0.324$  (top panels) and  $\epsilon = 0.33$  (bottom panels). For each case, results are shown for the surfactant-free and the surfactant-laden cases with  $\beta = 0.5$  and  $\beta_s = 0.9$  (columns one to three, respectively). For  $\epsilon = 0.324$ , the surfactant-free case exhibits a smooth flow separation near the wave crest, forming a broad region of negative  $\omega_y$  loosely coupled to the interface (see figure 9a). At moderate elasticity number  $\beta_s = 0.5$ , a distinct interfacial shear layer forms beneath the interface due to Marangoni-

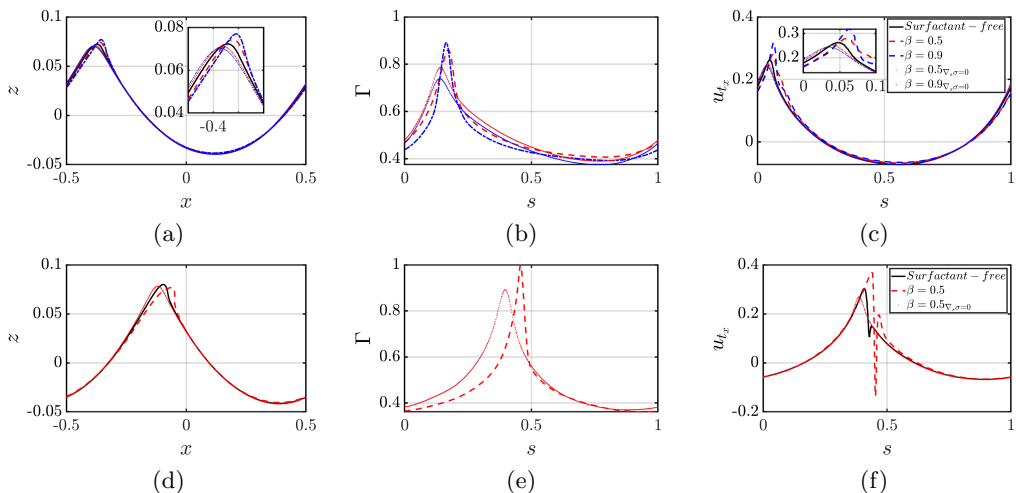


Figure 8: Two-dimensional projections of the interface location,  $\Gamma$ , and  $u_{tx}$  are shown in columns one through three. The top row (panels a-c) corresponds to  $\epsilon = 0.324$  at time  $t = 3.6$ , while the bottom row (panels d-f) corresponds to  $\epsilon = 0.33$  at time  $t = 4.4$ . For comparison, we also include cases in which Marangoni stresses have been deactivated by setting  $\nabla_s \sigma = 0$ .

driven flow, characterized by adjacent bands of positive and negative  $\omega_y$  straddling the interface, a signature of Marangoni-driven vorticity generation (see figure 9b). At higher elasticity  $\beta_s = 0.9$ , this vorticity layer becomes more localized and antisymmetric, and a secondary vorticity layer of opposite sign develops beneath the interface, a feature absent in the surfactant-free case. For the slightly larger steepness ( $\epsilon = 0.33$ ), separation is more abrupt, and early vortex roll-up occurs near the crest (see figure 9d). The presence of surfactant significantly amplifies these effects. The interfacial shear layer strengthens, and the vorticity becomes more intense and confined in regions of high  $\Gamma$  (see figure 9e,f). At  $\beta_s = 0.9$ , negative vorticity detaches from the interface, as the wave has started overturning with the generation of larger velocity gradients. The recirculation region shifts downstream and elongates, reflecting the influence of surfactants. Together, these results show that the presence of surfactant induces vorticity production and transforms a diffuse viscous shear layer into a localized dipole structure and ultimately triggers vorticity detachment and interface deformation.

Finally, we examine the role of Marangoni stresses in the generation of vorticity at the gas-liquid interface. Vorticity production at free surfaces has been the subject of several studies (Longuet-Higgins 1992; Cresswell & Morton 1995; Peck & Sigurdson 1998; Lundgren & Koumoutsakos 1999; Brøns *et al.* 2014; Constante-Amores *et al.* 2021a), and is particularly relevant in air-water systems where the free-surface approximation is appropriate. In this work, we adopt a two-dimensional version of the generalized formulation derived by Constante-Amores *et al.* (2023a), who described the evolution of circulation at a deformable interface within a three-dimensional control volume in the presence of surfactants. For brevity, we present only the final form of the governing equation used in the analysis in the main text; a full derivation of the two-dimensional

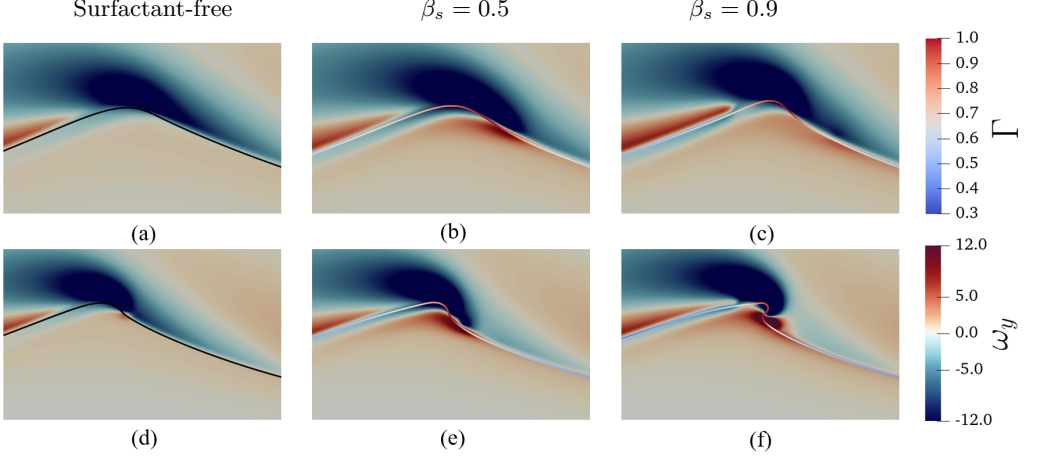


Figure 9: Two-dimensional representation of the interfacial location (colored by  $\Gamma$ ) overlaid with the spanwise vorticity component  $\omega_y$  in the  $(x - z)$  plane. Panels (a–c) correspond to  $\epsilon = 0.324$  at  $t = 4.2$ , while panels (d–f) correspond to  $\epsilon = 0.33$  at  $t = 4.0$ . Columns from left to right represent the surfactant-free case,  $\beta_s = 0.5$ , and  $\beta_s = 0.9$ , respectively.

form is provided in Appendix. The circulation is given by

$$\begin{aligned} \frac{D}{Dt} \left( \int_A \omega \, dA + \int_a^b [[\mathbf{u} \cdot \mathbf{t}]] \, ds \right) &= \oint_C \nu \nabla \omega \cdot \mathbf{n}_c \, ds - \int_a^b \kappa [(\mathbf{u} \cdot \mathbf{n})(\mathbf{u} \cdot \mathbf{t})] \, ds \\ &\quad + \frac{1}{2} \int_a^b \frac{\partial}{\partial s} [(\mathbf{u} \cdot \mathbf{n})^2] \, ds - \int_a^b \frac{\partial}{\partial s} \left[ \left[ \frac{p}{\rho} \right] \right] \, ds. \end{aligned} \quad (3.1)$$

Equation 3.1 describes the rate of change of circulation within a two dimensional control volume intersecting an arbitrary fluid interface of area  $A$  separating two fluids with different material properties. The left-hand side consists of two terms: the integral of vorticity over  $A$ , and the circulation jump along the curve from  $a$  to  $b$ , represented by the jump in tangential velocity  $[[\mathbf{u} \cdot \mathbf{t}]]$ . However, under the assumption of velocity continuity across the interface in both normal and tangential directions, and given that the unit normal  $\mathbf{n}$  and tangential  $\mathbf{t}$  vectors are identical on either side of the interface, the jump in tangential velocity  $[[\mathbf{u} \cdot \mathbf{t}]]$  vanishes. Similarly, the second term on the right-hand side involving the jump of the product  $(\mathbf{u} \cdot \mathbf{n})(\mathbf{u} \cdot \mathbf{t})$  and the third term involving the jump of  $(\mathbf{u} \cdot \mathbf{n})^2$  also vanish. Therefore, the second term on the left-hand side and the second and third terms on the right-hand side of equation 3.1 are identically zero.

The last RHS term of equation 3.1 involves a jump in the pressure across the interface. Taking into account the jump in the normal stress condition at the interface, we express  $\partial[[p/\rho]]/\partial s$  as

$$\frac{\partial}{\partial s} \left[ \left[ \frac{p}{\rho} \right] \right] = -\frac{1}{\rho_1} \frac{\partial}{\partial s} (\kappa \sigma) - \frac{2}{\rho_1} \left[ \mu \left( \frac{\partial^2}{\partial s^2} (\mathbf{u} \cdot \mathbf{t}) + \frac{\partial}{\partial s} (\kappa (\mathbf{u} \cdot \mathbf{n})) \right) \right] + \left[ \left[ \frac{1}{\rho} \right] \right] \frac{\partial p_2}{\partial s}. \quad (3.2)$$

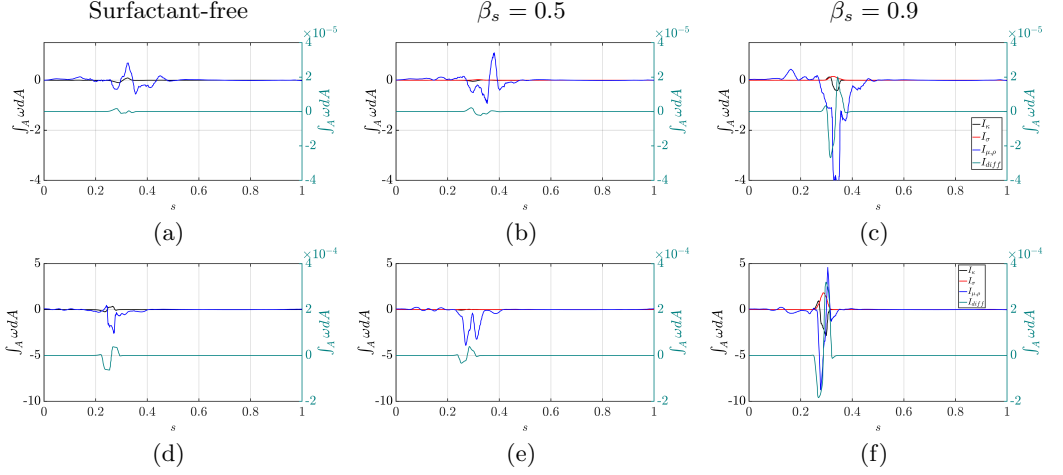


Figure 10: Two-dimensional representation of circulation generation mechanisms along the interface in the  $(x-z)$  plane. Panels (a–c) correspond to  $\epsilon = 0.324$  at  $t = 4.2$ , and panels (d–f) to  $\epsilon = 0.33$  at  $t = 4.0$ . Columns from left to right show the surfactant-free case,  $\beta_s = 0.5$ , and  $\beta_s = 0.9$ , respectively.

Therefore, the final expression for the circulation is that

$$\begin{aligned} \frac{D}{Dt} \left( \int_A \omega dA \right) = & \oint_C \nu \nabla \omega \cdot \mathbf{n} ds + \int_a^b \frac{\sigma}{\rho_2} \frac{\partial \kappa}{\partial s} ds + \int_a^b \frac{\kappa}{\rho_2} \frac{\partial \sigma}{\partial s} ds \\ & + \int_a^b \left( \frac{2}{\rho_1} [[\mu]] \left( \frac{\partial^2}{\partial s^2} (\mathbf{u} \cdot \hat{\mathbf{t}}) + \frac{\partial}{\partial s} (\kappa (\mathbf{u} \cdot \hat{\mathbf{n}})) \right) - [[\frac{1}{\rho}]] \frac{\partial p_2}{\partial s} \right) ds, \end{aligned} \quad (3.3)$$

where the terms of the RHS represent mechanisms that drive the net evolution of circulation. These include the viscous diffusion, curvature gradients, surface tension gradients along the interface (including Marangoni effects), jumps in viscosity and pressure across the interface.

Figure 10 shows the RHS terms of equation 3.3, evaluated along the arclength  $s$  in an  $(x-z)$  plane located at the centerline of the domain, for the two spilling-like regimes considered in this work,  $\epsilon = 0.324$  (top panels) and  $\epsilon = 0.33$  (bottom panels). For each case, results are shown for the surfactant-free and the surfactant-laden cases with  $\beta = 0.5$  and  $\beta_s = 0.9$  (columns one to three, respectively). This allows identification of the dominant physical mechanisms contributing to circulation generation. The viscous diffusion term is negligible in all conditions, confirming that interfacial mechanisms dominate circulation production. Across all cases, the primary contributor is the term associated with jumps in viscosity and density, which is consistent with the large density ratio in the system. Notably, the magnitude of this term increases in the presence of surfactants, indicating more intense interfacial activity. Contributions from surface tension gradients (Marangoni stresses) become significant only at the largest elasticity number, and they are spatially localized near regions of strong gradients in  $\Gamma$ , particularly along the wave crest.



## 4. Conclusions

We present a detailed analysis of the effect of insoluble surfactants on wave breaking dynamics in both regular and spilling regimes, using high-resolution three-dimensional simulations. At  $We = 100$  and  $Re = 10^4$ , we explore how wave steepness modulates the flow in the presence of surfactants. The hybrid front-tracking/level-set method employed enables accurate coupling of inertia, capillarity, interfacial diffusion, and Marangoni stresses arising from surfactant-induced surface tension gradients. We find that surfactants have minimal impact on regular breakers, which retain similar shapes to the surfactant-free case, though a gradual interfacial rigidification is observed at longer times. In contrast, for spilling breakers, increasing elasticity induces a marked shift in dynamics, culminating in a transition to plunging behavior. Our analysis demonstrates that surfactant-induced Marangoni stresses, rather than surface tension reduction, are solely responsible for driving the transition. We also show that surfactants generate interfacial vorticity through Marangoni stresses driven by surfactant concentration gradients.

Future studies should extend the present analysis beyond the regular and spilling regimes into the fully plunging regime, where bubble entrainment and droplet ejection result from the dynamics. Capturing these processes requires that all relevant length and time scales be resolved, making adaptive mesh refinement indispensable. Higher Reynolds numbers and greater wave steepness must also be explored to reproduce realistic ocean conditions. In addition, incorporating soluble surfactants, with full adsorption/desorption kinetics and bulk transport, would introduce chemical timescales that could either damp or amplify wave breaking events.

Declaration of Interests. The authors report no conflict of interest.

## Acknowledgments

This research used the Delta advanced computing and data resource which is supported by the National Science Foundation (award OAC 2005572) and the State of Illinois. CRCA acknowledges with gratitude O. K. Matar for insightful discussions on vorticity production, and L. Kahouadji for initial discussions. D.J. and J.C. acknowledge support through HPC/AI computing time at the Institut du Developpement et des Ressources en Informatique Scientifique (IDRIS) of the Centre National de la Recherche Scientifique (CNRS), coordinated by GENCI (Grand Equipement National de Calcul Intensif) grant 2025 A0182B06721. The numerical simulations were performed with code BLUE (Shin *et al.* 2017)

## Appendix: Vorticity generation in two-dimensional flows

### Circulation

Before we examine the sources of vorticity flux near an interface, we must first consider the case of a single fluid and the vorticity equation which is given by

$$\frac{\partial \boldsymbol{\omega}}{\partial t} + \mathbf{u} \cdot \nabla \boldsymbol{\omega} + \boldsymbol{\omega} \cdot \nabla \mathbf{u} = \nu \nabla^2 \boldsymbol{\omega}. \quad (4.1)$$

Now, for a 2D flow,  $\boldsymbol{\omega} \cdot \nabla \mathbf{u} = 0$  since  $\nabla \mathbf{u}$  exists only in the  $(x, y)$  plane whereas  $\boldsymbol{\omega} = (0, 0, \omega)$ . Thus, Eq. (4.1) can be expressed as a 2D equation for the scalar quantity  $\omega$ :

$$\frac{D\omega}{Dt} = \nu \nabla^2 \omega. \quad (4.2)$$

From Stokes's theorem, we can write  $\oint_C \mathbf{v} \cdot d\mathbf{s} = \int_A (\nabla \times \mathbf{v}) \cdot d\mathbf{a}$  for any vector  $\mathbf{v}$  where  $d\mathbf{s}$  is an infinitesimal displacement along the arclength on a contour  $C$  that encloses a simply connected<sup>†</sup> area  $A$  in the fluid and  $d\mathbf{a} = \mathbf{e}_k dA$  represents an infinitesimal region in this area;  $\mathbf{e}_k$  points into the page perpendicularly to the  $(x, y)$  plane. Thus, if we set  $\mathbf{v} = \mathbf{u}$  then

$$\oint_C \mathbf{u} \cdot d\mathbf{s} = \int_A (\nabla \times \mathbf{u}) \cdot \mathbf{e}_k dA = \int_A \boldsymbol{\omega} \cdot \mathbf{e}_k dA = \int_A \omega dA \equiv \Gamma_A, \quad (4.3)$$

which relates the *total circulation*  $\Gamma_A$  to  $\omega$ . By taking a total derivative of  $\Gamma_A$  and making use of Eq. (4.2), we can write

$$\frac{D\Gamma_A}{Dt} = \frac{D}{Dt} \int_A \omega dA = \int_A \frac{D\omega}{Dt} dA = \int_A \nu \nabla^2 \omega dA. \quad (4.4)$$

Using the Divergence Theorem, the final term on the LHS of this equation can re-expressed as follows

$$\int_A \nu \nabla^2 \omega dA = \int_A \nabla \cdot (\nu \nabla \omega) dA = \oint_C \mathbf{n}_c \cdot (\nu \nabla \omega) ds, \quad (4.5)$$

where  $\mathbf{n}_c$  is the outward-pointing unit normal to the contour  $C$ . As a result, the total rate of change of circulation in area  $A$ ,  $\Gamma_A$ , becomes

$$\frac{D\Gamma_A}{Dt} = \frac{D}{Dt} \int_A \omega dA = \oint_C \nu \nabla \omega \cdot \mathbf{n}_c ds. \quad (4.6)$$

This is an important equation which shows that the change in circulation results directly from the flux of vorticity from the boundary (characterised by the contour  $C$ ).

#### Near-interface Vorticity jump

We consider the case of two fluids separated by an interface. In order to evaluate the LHS of Eq. (4.6), we follow an approach that relies on a construction similar to that represented by Fig. 2 in Brøns *et al.* (2014). This is necessary because the area  $A$  is no longer simply connected but is instead divided because of the presence of the interface. With reference to Fig 2 in Brøns *et al.* (2014), we write

$$\frac{D}{Dt} \int_{A_1 \cup A_2} \omega dA = \int_{C_1} \nu_1 \nabla \omega_1 \cdot \mathbf{n}_c ds + \int_{C_2} \nu_2 \nabla \omega_2 \cdot \mathbf{n}_c ds + \int_{C'_1} \nu_1 \nabla \omega_1 \cdot \mathbf{n}_c ds + \int_{C'_2} \nu_2 \nabla \omega_2 \cdot \mathbf{n}_c ds. \quad (4.7)$$

Here, we distinguish between the normal to the contour  $C$ ,  $\mathbf{n}_c$ , and that to the interface  $I$ ,  $\mathbf{n}$ .

We now let  $\mathbf{n}_c \rightarrow -\mathbf{n}$  from the fluid 2 side, and  $\mathbf{n}_c \rightarrow \mathbf{n}$  from the fluid 1 side, which results in

$$\frac{D}{Dt} \int_{A_1 \cup A_2} \omega dA = \int_{C_1} \nu_1 \nabla \omega_1 \cdot \mathbf{n}_c ds + \int_{C_2} \nu_2 \nabla \omega_2 \cdot \mathbf{n}_c ds + \int_{C'_1} \nu_1 \nabla \omega_1 \cdot \mathbf{n} ds - \int_{C'_2} \nu_2 \nabla \omega_2 \cdot \mathbf{n} ds. \quad (4.8)$$

We note that in region  $A_1$ , we march in an anti-clockwise direction along contour  $C'_1$  where  $\mathbf{n}_c$  is aligned with  $\mathbf{n}$  and then along contour  $C_1$ . In region  $A_2$ , we march along

<sup>†</sup> Note that this becomes important below when we consider the case of two fluids separated by an interface.

contour  $C_2$  in an anti-clockwise direction and then along contour  $C'_2$  where  $\mathbf{n}_c$  points out of fluid 2 into fluid 1 in a direction opposite to that of  $\mathbf{n}$ ; the latter explains the minus sign in the fourth term of Eq. (4.8).

We now let the contours  $C'_1$  and  $C'_2$  approach the interface  $I$  so that the union of  $A_1$  and  $A_2$  approaches  $A$ , i.e.  $A_1 \cup A_2 \rightarrow A$ , which leads to

$$\frac{D}{Dt} \int_A \omega dA = \oint_C \nu \nabla \omega \cdot \mathbf{n}_c ds - \left( \int_I \nu_2 \nabla \omega_2 \cdot \mathbf{n} ds - \int_I \nu_1 \nabla \omega_1 \cdot \mathbf{n} ds \right). \quad (4.9)$$

By introducing the notation  $[[q]] = q_2 - q_1$  for the jump across the interface of a quantity  $q$ , this equation can be re-expressed as follows

$$\frac{D}{Dt} \int_A \omega dA = \oint_C \nu \nabla \omega \cdot \mathbf{n}_c ds - \int_a^b [[\nu \nabla \omega \cdot \mathbf{n}]] ds. \quad (4.10)$$

Equation (4.10) illustrates the contribution of the jump in the vorticity flux across the interface to the rate of change of the circulation. We can calculate this jump by using

$$\frac{D}{Dt}(\mathbf{u} \cdot \mathbf{t}) + \kappa(\mathbf{u} \cdot \mathbf{n})(\mathbf{u} \cdot \mathbf{t}) - \frac{1}{2} \frac{\partial}{\partial s}(\mathbf{u} \cdot \mathbf{n})^2 + \frac{\nabla p}{\rho} \cdot \mathbf{t} = \nu \nabla \omega \cdot \mathbf{n}, \quad (4.11)$$

which comes from Eq. (23) in Lundgren & Koumoutsakos (1999) and Eq. (2.10) in Brøns *et al.* (2014). Then, we have

$$\frac{D}{Dt} [[\mathbf{u} \cdot \mathbf{t}]] + \kappa [[(\mathbf{u} \cdot \mathbf{n})(\mathbf{u} \cdot \mathbf{t})]] + \frac{\partial}{\partial s} \left[ \left[ \left( \frac{p}{\rho} \right) \right] \right] - \frac{1}{2} \frac{\partial}{\partial s} [[(\mathbf{u} \cdot \mathbf{n})^2]] = [[\nu \nabla \omega \cdot \mathbf{n}]]; \quad (4.12)$$

here, we have used the fact that  $\mathbf{t} \cdot \nabla = (\partial/\partial s)$ . Substitution of Eq. (4.12) into Eq. (4.10) leads to

$$\begin{aligned} \frac{D}{Dt} \left( \int_A \omega dA + \int_a^b [[\mathbf{u} \cdot \mathbf{t}]] ds \right) &= \oint_C \nu \nabla \omega \cdot \mathbf{n}_c ds - \int_a^b \kappa [[(\mathbf{u} \cdot \mathbf{n})(\mathbf{u} \cdot \mathbf{t})]] ds \\ &\quad + \frac{1}{2} \int_a^b \frac{\partial}{\partial s} [[(\mathbf{u} \cdot \mathbf{n})^2]] ds - \int_a^b \frac{\partial}{\partial s} \left[ \left[ \left( \frac{p}{\rho} \right) \right] \right] ds. \end{aligned} \quad (4.13)$$

Equation (4.13) involves a jump in the pressure across the interface. To make progress, we must first consider the jump in the normal stress condition at the interface expressed by

$$-p_1 + \mu_1 \mathbf{n} \cdot \mathbf{D}_1 \cdot \mathbf{n} + \kappa \sigma = -p_2 + \mu_2 \mathbf{n} \cdot \mathbf{D}_2 \cdot \mathbf{n}, \quad (4.14)$$

in which  $\sigma$  represents the interfacial tension and  $\mu_1$  and  $\mu_2$  the dynamic viscosities of fluids 1 and 2, respectively. Rearranging Eq. (4.14) yields

$$[[p]] = -\kappa \sigma - 2 \left[ \left[ \mu \left( \frac{\partial}{\partial s}(\mathbf{u} \cdot \mathbf{t}) + \kappa(\mathbf{u} \cdot \mathbf{n}) \right) \right] \right]; \quad (4.15)$$

here, we have made use of

$$\mathbf{n} \cdot \mathbf{D} \cdot \mathbf{n} = -2 \frac{\partial}{\partial s}(\mathbf{u} \cdot \mathbf{t}) - 2(\mathbf{u} \cdot \mathbf{n})\kappa. \quad (4.16)$$

Now, we re-express  $[[p/\rho]]$  as follows

$$\begin{aligned} [[\frac{p}{\rho}]] &= \frac{p_2}{\rho_2} - \frac{p_1}{\rho_1} = \frac{p_2}{\rho_2} - \frac{p_2}{\rho_1} + \frac{p_2}{\rho_1} - \frac{p_1}{\rho_1} \\ &= p_2 \left( \frac{1}{\rho_2} - \frac{1}{\rho_1} \right) + \frac{1}{\rho_1} (p_2 - p_1) \\ &= p_2 [[\frac{1}{\rho}]] + \frac{[[p]]}{\rho_1}, \end{aligned} \quad (4.17)$$

from which we get that

$$\frac{\partial}{\partial s} [[\frac{p}{\rho}]] = -\frac{1}{\rho_1} \frac{\partial}{\partial s} (\kappa \sigma) - \frac{2}{\rho_1} [[\mu \left( \frac{\partial^2}{\partial s^2} (\mathbf{u} \cdot \mathbf{t}) + \frac{\partial}{\partial s} (\kappa [\mathbf{u} \cdot \mathbf{n}]) \right)]] + [[\frac{1}{\rho}]] \frac{\partial p_2}{\partial s}. \quad (4.18)$$

## REFERENCES

- AMBRAVANESWARAN, B. & BASARAN, O.A. 1999 Effects of insoluble surfactants on the nonlinear deformation and breakup of stretching liquid bridges. *Phys. Fluids* **11** (5), 997–1015.
- BATCHVAROV, A., KAHOUADJI, L., CONSTANTE-AMORES, C.R., NORÕES GONÇALVES, G.F., SHIN, S., CHERGUI, J., JURIC, D., CRASTER, R.V. & MATAR, O.K. 2021 Three-dimensional dynamics of falling films in the presence of insoluble surfactants. *J. Fluid Mech.* **906**, A16.
- BATCHVAROV, A., KAHOUADJI, L., MAGNINI, M., CONSTANTE-AMORES, C. R., CRASTER, R. V., SHIN, S., CHERGUI, J., JURIC, D. & MATAR, O. K. 2020 Effect of surfactant on elongated bubbles in capillary tubes at high reynolds number. *Phys. Rev. Fluids* **5**, 093605.
- BRØNS, M., THOMPSON, M.C., LEWEKE, T. & HOURIGAN, K. 2014 Vorticity generation and conservation for two-dimensional interfaces and boundaries. *J. Fluid Mech.* **758**, 63–93.
- CENICEROS, H.D. 2003 The effects of surfactants on the formation and evolution of capillary waves. *Phys. Fluids* **15** (1), 245–256.
- CHEN, G., KHARIF, C., ZALESKI, S. & LI, J. 1999 Two-dimensional navier–stokes simulation of breaking waves. *Phys. Fluids* **11** (1), 121–133.
- CONSTANTE-AMORES, C., ABADIE, T., KAHOUADJI, L., SHIN, S., CHERGUI, J., JURIC, D., CASTREJÓN-PITA, A. & MATAR, O. 2023a Direct numerical simulations of turbulent jets: vortex–interface–surfactant interactions. *J. Fluid Mech.* **955**, A42.
- CONSTANTE-AMORES, C., BATCHVAROV, A., KAHOUADJI, L., SHIN, S., CHERGUI, J., JURIC, D. & MATAR, O. 2021a Role of surfactant-induced marangoni stresses in drop-interface coalescence. *J. Fluid Mech.* **925**, A15.
- CONSTANTE-AMORES, C., CHERGUI, J., SHIN, S., JURIC, D., CASTREJÓN-PITA, J. & CASTREJÓN-PITA, A. 2022 Role of surfactant-induced marangoni stresses in retracting liquid sheets. *J. Fluid Mech.* **949**, A32.
- CONSTANTE-AMORES, C.R., KAHOUADJI, L., BATCHVAROV, A., S., S., CHERGUI, J., JURIC, D. & MATAR, O.K. 2020 Dynamics of retracting surfactant-laden ligaments at intermediate ohnesorge number. *Phys. Rev. Fluids* **5**, 084007.
- CONSTANTE-AMORES, C., KAHOUADJI, L., BATCHVAROV, A., SHIN, S., CHERGUI, J., JURIC, D. & MATAR, O. 2021b Direct numerical simulations of transient turbulent jets: vortex–interface interactions. *J. Fluid Mech.* **922**, A6.
- CONSTANTE-AMORES, C., KAHOUADJI, L., BATCHVAROV, A., SHIN, S., CHERGUI, J., JURIC, D. & MATAR, O. 2021c Dynamics of a surfactant-laden bubble bursting through an interface. *J. Fluid Mech.* **911**, A57.
- CONSTANTE-AMORES, CR, KAHOUADJI, L, SHIN, S, CHERGUI, J, JURIC, D, CASTREJÓN-PITA, JR, MATAR, OK & CASTREJÓN-PITA, AA 2023b Impact of droplets onto surfactant-laden thin liquid films. *J. Fluid Mech.* **961**, A8.
- CRASTER, R.V., MATAR, O.K. & PAPAGEORGIOU, D.T. 2002 Pinchoff and satellite formation in surfactant covered viscous threads. *Phys. Fluids* **14** (4), 1364–1376.

- CRESSWELL, R.W. & MORTON, B.R. 1995 Drop-formed vortex rings-the generation of vorticity. *Phys. Fluids* **7** (6), 1363–1370.
- DEIKE, L. 2022 Mass transfer at the ocean–atmosphere interface: the role of wave breaking, droplets, and bubbles. *Annu. Rev. Fluid Mech.* **54** (1), 191–224.
- DEIKE, L., GHABACHE, E., LIGER-BELAIR, G., DAS, A. K., ZALESKI, S., POPINET, S. & SÉON, T. 2018 Dynamics of jets produced by bursting bubbles. *Phys. Rev. Fluids* **3**, 013603.
- DEIKE, LUC, MELVILLE, W KENDALL & POPINET, STÉPHANE 2016 Air entrainment and bubble statistics in breaking waves. *J. Fluid Mech.* **801**, 91–129.
- DEIKE, L., POPINET, S. & MELVILLE, W.K. 2015 Capillary effects on wave breaking. *J. Fluid Mech.* **769**, 541–569.
- DI GIORGIO, S., PIROZZOLI, S. & IAFRATI, A. 2022 On coherent vortical structures in wave breaking. *J. Fluid Mech.* **947**, A44.
- DI GIORGIO, S., PIROZZOLI, S. & IAFRATI, A. 2024 Air entrainment and gas transfer processes in wave breaking events. *arXiv preprint arXiv:2412.20576*.
- DUNCAN, J.H. 2001 Spilling breakers. *Annu. Rev. Fluid Mech.* **33** (1), 519–547.
- DUNCAN, J.H., QIAO, H., PHILOMIN, V. & WENZ, A. 1999 Gentle spilling breakers: crest profile evolution. *J. Fluid Mech.* **379**, 191–222.
- ERININ, M., LIU, C., LIU, X., MOSTERT, W., DEIKE, L. & DUNCAN, J. 2023 The effects of surfactants on plunging breakers. *J. Fluid Mech.* **972**, R5.
- GARBE, C.S., RUTGERSSON, A., BOUTIN, J., DE LEEUW, G., DELILLE, B., FAIRALL, C.W., GRUBER, N., HARE, J., HO, D.T., JOHNSON, M.T. & OTHERS 2014 Transfer across the air-sea interface. *Ocean-Atmos. Interact. Gases Part.* pp. 55–112.
- GRUE, J. & FRUCTUS, D. 2010a Model for fully nonlinear ocean wave simulations derived using fourier inversion of integral equations in 3d. In *Advances in numerical simulation of nonlinear water waves*, pp. 1–42. World Scientific.
- GRUE, JOHN & FRUCTUS, DORIAN 2010b *MODEL FOR FULLY NONLINEAR OCEAN WAVE SIMULATIONS DERIVED USING FOURIER INVERSION OF INTEGRAL EQUATIONS IN 3D*, pp. 1–42.
- HU, Y., LIU, C., YANG, X. & HU, C. 2024 Numerical investigation of the plunging breaker under various wave slopes: Characteristics of spray droplets and air entrainment. *Ocean Eng.* **303**, 117635.
- IAFRATI, A. 2009 Numerical study of the effects of the breaking intensity on wave breaking flows. *J. Fluid Mech.* **622**, 371–411.
- KAMAT, P.M., WAGONER, B.W., THETE, S.S. & BASARAN, O.A. 2018 Role of marangoni stress during breakup of surfactant-covered liquid threads: Reduced rates of thinning and microthread cascades. *Phys. Rev. Fluids* **3**, 043602.
- LANDAU, L.D. & LIFSHITZ, E.M. 1987 *Fluid Mechanics: Volume 6*, , vol. 6. Elsevier.
- LAPHAM, G.S. 1998 *Wave-surfactant interaction*. University of Michigan.
- LAXAGUE, N.J., ZAPPA, C.J., SOUMYA, S. & WURL, O. 2024 The suppression of ocean waves by biogenic slicks. *J. R. Soc. Interface* **21** (220), 20240385.
- LIAO, Y., FRANCES, E.I. & BASARAN, O.A. 2006 Deformation and breakup of a stretching liquid bridge covered with an insoluble surfactant monolayer. *Phys. Fluids* **18** (2).
- LIU, C., ERININ, M., LIU, X. & DUNCAN, J. 2025 The effect of surfactants on droplet generation in a plunging breaker. *J. Fluid Mech.* **1009**, A31.
- LIU, X. & DUNCAN, J.H. 2003 The effects of surfactants on spilling breaking waves. *Nature* **421** (6922), 520–523.
- LIU, X. & DUNCAN, J.H. 2006 An experimental study of surfactant effects on spilling breakers. *J. Fluid Mech.* **567**, 433–455.
- LIU, X. & DUNCAN, J.H. 2007 Weakly breaking waves in the presence of surfactant micelles. *Phys. Rev. E* **76** (6), 061201.
- LONGUET-HIGGINS, M.S. 1992 Capillary rollers and bores. *J. Fluid Mech.* **240**, 659–679.
- LUNDGREN, T. & KOUMOUTSAKOS, P. 1999 On the generation of vorticity at a free surface. *J. Fluid Mech.* **382**, 351–366.
- MA, T., HESSENKEMPER, H., LUCAS, D. & BRAGG, A.D. 2023 Effects of surfactants on bubble-induced turbulence. *J. Fluid Mech.* **970**, A13.
- MANIKANTAN, H. & SQUIRES, T.M. 2020 Surfactant dynamics: hidden variables controlling fluid flows. *J. Fluid Mech.* **892**, P1.

- MELVILLE, W.K. 1996 The role of surface-wave breaking in air-sea interaction .
- MOSTERT, W. & DEIKE, L. 2020 Inertial energy dissipation in shallow-water breaking waves. *J. Fluid Mech.* **890**, A12.
- MOSTERT, WOUTER, POPINET, STÉPHANE & DEIKE, LUC 2022 High-resolution direct simulation of deep water breaking waves: transition to turbulence, bubbles and droplets production. *J. Fluid Mech.* **942**, A27.
- PECK, B. & SIGURDSON, L. 1998 On the kinetics at a free surface. *IMA J. Appl. Math.* **61** (1), 1–13.
- QIAO, H. & DUNCAN, J.H. 2001 Gentle spilling breakers: crest flow-field evolution. *J. Fluid Mech.* **439**, 57–85.
- RAPP, R.J. & MELVILLE, W.K. 1990 Laboratory measurements of deep-water breaking waves. *Philosophical Transactions of the Royal Society of London. Series A, Mathematical and Physical Sciences* **331** (1622), 735–800.
- SHIN, S., CHERGUI, J. & JURIC, D. 2017 A solver for massively parallel direct numerical simulation of three-dimensional multiphase flows. *J. Mech. Sci. Tech.* **31**, 1739–1751.
- SHIN, S., CHERGUI, J., JURIC, D., KAHOUADJI, L., MATAR, O. K. & CRASTER, R. V. 2018 A hybrid interface tracking – level set technique for multiphase flow with soluble surfactant. *J. Comp. Phys.* **359**, 409–435.
- STONE, H.A. 1990 A simple derivation of the time-dependent convective-diffusion equation for surfactant transport along a deforming interface. *Phys. Fluids A: Fluid Dynamics* **2** (1), 111–112.
- TAKAGI, S. & MATSUMOTO, Y. 2011 Surfactant effects on bubble motion and bubbly flows. *Annu. Rev. Fluid Mech.* **43** (1), 615–636.
- WANG, Z., YANG, J. & STERN, F. 2016 High-fidelity simulations of bubble, droplet and spray formation in breaking waves. *J. Fluid Mech.* **792**, 307–327.
- WEE, H., WAGONER, B.W., KAMAT, P.M. & BASARAN, O.A. 2020 Effects of surface viscosity on breakup of viscous threads. *Phys. Rev. Lett.* **124** (20), 204501.
- WHITHAM, G.B. 2011 *Linear and nonlinear waves*. John Wiley & Sons.